A Hybrid Modulation Featuring Two-phase Clamped Discontinuous PWM and Zero Voltage Switching for 99% Efficient DC-Type EV Charger

Xu, Junzhong; Soeiro, Thiago Batista; Wang, Yong; Gao, Fei; Tang, Houjun; Bauer, Pavol

DOI
10.1109/TVT.2021.3133647

Publication date
2022

Document Version
Final published version

Published in
IEEE Transactions on Vehicular Technology

A Hybrid Modulation Featuring Two-Phase Clamped Discontinuous PWM and Zero Voltage Switching for 99% Efficient DC-Type EV Charger

Junzhong Xu, *Member, IEEE*, Thiago Batista Soeiro, *Senior Member, IEEE*, Yong Wang, *Member, IEEE*, Fei Gao, *Member, IEEE*, Houjun Tang, and Pavol Bauer, *Senior Member, IEEE*

***Abstract*—Two-stage AC-DC converters are considered as a prominent solution for DC-type electric vehicle (EV) chargers. However, this kind of architecture suffers from high switching losses with large heatsink and DC-link capacitor volume. To relieve this issue, this paper presents a new hybrid modulation for DC-type EV chargers, where a two-phase clamped discontinuous pulse-width-modulation (DPWM) in the front-end circuit is cooperated with the variable frequency triangular-current-mode (TCM) zero voltage switching (ZVS) or its simplified implementation, i.e., boundary-ZVS (B-ZVS) strategy, in the back-end circuit. The former can stop the switching actions in the front-end stage during two-thirds of the grid period, while the AC currents are at their highest values, which can yield to the best switching loss reduction and deliver high power factor operation. Besides, TCM-ZVS or B-ZVS modulations can achieve ZVS turn-on action for all semiconductors during all operating range in the DC-DC stage to further reduce the power losses on the semiconductors. With such characteristics, the proposed strategies can reduce the switching losses of the system to the best extent, and thus allow an enhancement of the system power density by improving the power conversion efficiency. The proposed strategy is described, analyzed, validated, and benchmarked in a 5 kW SMD SiC MOSFET-based two-stage AC-DC converter. A 99% power efficiency can be achieved with the solution implementing the TCM-ZVS strategy at an output voltage of 400 V and rated power.**

***Index Terms*—Electric vehicle (EV), two-stage AC-DC converter, discontinuous pulse width modulation (DPWM), zero voltage switching (ZVS).**

I. Introduction

With the proliferation and development of electric vehicles (EVs) market, currently, most EVs can be charged at 50 kW and 400 V following the fast charging standards "CCS - up to 80 kW" and "CHAdeMO - approx. 50 kW" [1]–[5]. To meet these requirements, high power-level three-phase AC-DC converters for DC-type EV charging systems are in high demand, which in certain cases allow a bidirectional power flow and consequently improve the grid stability by feeding back power to the mains by using the EV batteries as a grid energy storage [6]–[8]. Therefore, the interest to the topology circuits and corresponding control scheme of the DC-type EV charger has gained many momenta in both industry and academia [9]–[14].

Since the variation of EV battery voltages for DC-type EV charger is particularly wide, e.g., for a Nissan Leaf the rated power has to be provided to a DC voltage ranging from 300 V to 400 V from an AC grid connection with peak line-to-line voltages ranging from 540 V to 560 V in the Chinese and European markets [6], a charger with Boost and Buck functionality [15]–[18] is needed. Consequently, the two-stage Buck + Boost or (Boost + Buck) converters are considered as prominent solutions [17]–[19]. In this paper, a suitable two-stage three-phase AC-DC converter with connection to the grid through a 50/60 Hz isolated transformer is studied, as shown in Fig. 1, where a three-phase Boost converter is followed by a DC-DC Buck converter. Herein, the front-end converter comprises a three-phase three-wire two-level six-switch voltage source rectifier (2L-VSR), which inherently features low complexity and low cost, and favors for the off-board EV charger [20], [21]. The back-end circuit works as a three-channel pulse-width-modulation (PWM) interleaved DC-DC Buck converter. This features enhanced loss distribution among the semiconductors or better current shared between the parallel circuits than the hard-paralleling of semiconductors [22]–[24]. Due to the large capacitor between the two converters, their control scheme are typically implemented to be decoupled, which means the front-end and the back-end stages are modulated independently.

Unfortunately, such a two-stage solution usually suffers from high switching losses with large heatsink and DC-link capacitor volume. To improve the power conversion efficiency, different discontinuous PWM (DPWM) strategies instead of traditional continuous PWM methods can be applied to optimize the switching losses in the front-end AC-DC circuit [25]–[30]. Conventional DPWM methods such as DPWM0, DPWM1,

Manuscript received April 5, 2021; revised October 20, 2021; accepted December 5, 2021. Date of publication December 9, 2021; date of current version February 14, 2022. This work was supported by the National Natural Science Foundation of China under Grant 51577118. The review of this article was coordinated by Prof. M. Kazerani. *(Corresponding author: Yong Wang.)*

Junzhong Xu, Yong Wang, Fei Gao, and Houjun Tang are with the Department of Electrical Engineering, Shanghai Jiao Tong University, Shanghai 200240, China, and also with the Key Laboratory of Control of Power Transmission and Conversion, Ministry of Education, Shanghai 200240, China (e-mail: junzhongxu@sjtu.edu.cn; wangyong75@sjtu.edu.cn; fei.gao@sjtu.edu.cn; hjtang@sjtu.edu.cn).

Thiago Batista Soeiro and Pavol Bauer are with the Department of Electrical Sustainable Energy, DCE&S group, Delft University of Technology, 2628 Delft, CD, The Netherlands (e-mail: T.BatistaSoeiro@tudelft.nl; p.bauer@tudelft.nl).

Digital Object Identifier 10.1109/TVT.2021.3133647

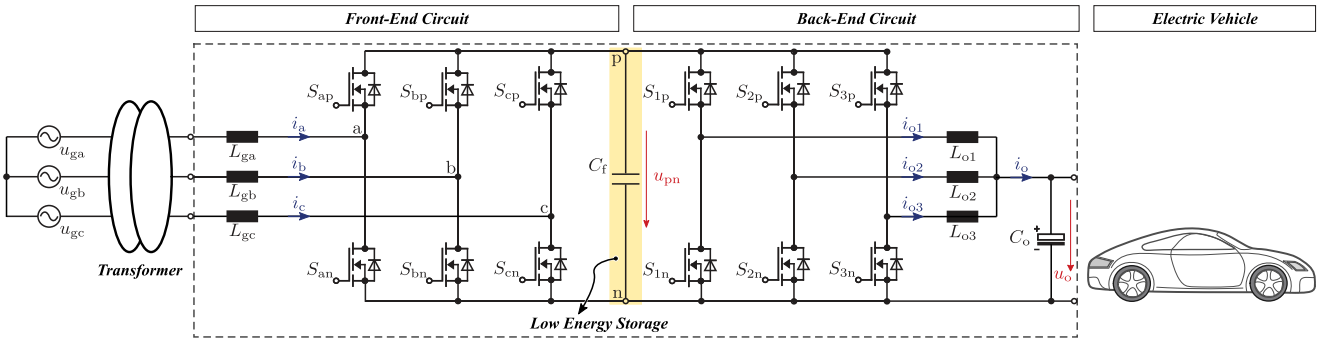

Fig. 1. Architecture of the DC-type EV charger.

DPWM2, DPWM3, DPWMMIN and DPWMMAX are summarized in [25], which can reduced the switching losses remarkably in comparison with the continuous PWM methods, i.e, sinusoidal PWM (SPWM), and space vector PWM (SVPWM). To further reduce the switching losses in a wide power factor range, a minimum-losses PWM method has been well studied in [26], [27], which distributes non-modulated segments variably according to the phase angle between reference voltage and input current. In [28], a direct digital technique-GDPWM (DDT-GDPWM) has been presented, which has the advantage of not requiring the load power factor information and low computation time. A scalar PWM method studied in [29], [30] has the capability to obtain the performance of minimum switching losses and to reduce common-mode voltage simultaneously. A synergetic control has been studied in two-level and three-level two-stage AC-DC converters, where only one-thirds of the grid period in the front-end stage is switched, i.e., 1/3 PWM [2], [3], [6], [7].

However, all of the aforementioned modulation strategies only focus on the switching losses reduction in the front-end stage and do not consider the losses optimization in the back-end stage or modulate the front- and back-end stages simultaneously. To fill this gap, a new hybrid modulation for DC-type EV charging systems to improve the converter overall efficiency is proposed in this paper, where the two-phase clamped DPWM in the front-end stage is cooperated with the variable frequency triangular-current-mode (TCM) zero-voltage-switching (ZVS) modulation and its simplified implementation called here the boundary-ZVS (B-ZVS) strategy in the back-end stage. Herein, the two-phase clamped DPWM method is implemented in the front-end stage, which yields to the best switching loss reduction in any known DPWM strategies especially at high power factor (HPF) operation. Moreover, ZVS turn-on feature can be achieved by variable frequency controlled TCM-ZVS or the B-ZVS in the back-end PWM interleaved DC-DC stage to further reduce the switching losses of the system. The ZVS turn-on strategies combined with symmetric PWM interleaved operation will also cancel out the high frequency harmonics proportional to the number of employed parallel circuits in both voltages and currents, lowering the root mean square (RMS) current across the DC capacitors $C_{\rm f}$ and $C_{\rm o}$. Through the proposed coupled modulation, a lager voltage ripple can be allowed in the DC-link, and thus a DC-link employing capacitor with low energy storage capability, e.g., an electrolytic capacitor-less DC-link, can be used as well. It is noted that to the best of authors' knowledge, so far no literature work has applied such a loss-optimization hybrid modulation in EV charging systems based on the presented circuit topology as shown in Fig. 1.

This paper contributes to the following points:

- A new hybrid modulation with two-phase clamped DPWM cooperated with the TCM-ZVS or B-ZVS strategy are proposed for the application of DC-type EV chargers.
- The detailed system operation and analytical semiconductor stresses modeling of the studied two-stage converter with different modulation strategies are presented.
- The benchmarking with the different hybrid modulations is performed in experiments.

The rest of this paper is organized as follows. In Section II, the explanation of the structural characteristics of the presented DC-type EV charger, modulation strategy featuring low switching losses and feedback control method are presented. In Section III, the analytical equations for semiconductor stresses are given. Finally, in Section IV, the studied hybrid modulation is evaluated and benchmarked against the conventional modulation in the simulation and a 5 kW SMD SiC MOSFET-based prototype.

II. Working Principle of the Proposed Hybrid Modulation

This section describes the basic operation of the EV battery charger system depicted in Fig. 1. As previously discussed, the front- and back-end circuits are connected to each other through a DC-link with low energy storage capability, which makes the operation of both circuits highly coupled to each other. Herein, the front-end AC-DC stage is composed of six active switches ($S_{x\rm p}$ and $S_{x\rm n}, x \in a, b, c$), and the back-end interleaved DC-DC stage is structured by another six active switches ($S_{i\rm p}$ and $S_{i\rm n}, i \in 1, 2, 3$), which are connected with the front-end stage via the DC-link capacitor $C_{\rm f}$; u_{pn} is the DC-link voltage; u_{gx} and i_x are the AC voltage and current, respectively; L_{gx} is the input inductor; $u_{\rm o}$ and $i_{\rm o}$ are the output voltage and current, and i_{oi} is the current passing through the output inductor L_{oi}; $C_{\rm o}$ is the output capacitor.

In fact, the circuit operates similarly to a single stage three-phase Buck-type AC-DC converter [31]–[33], where the two

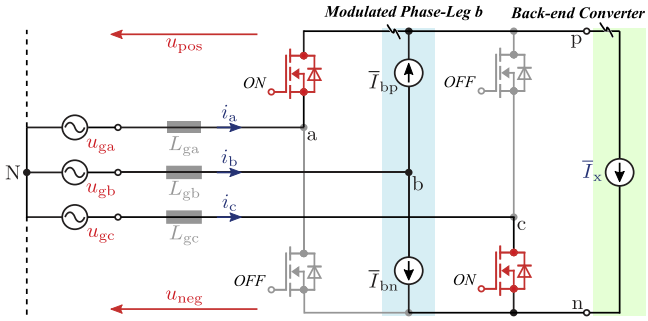

Fig. 2. Equivalent circuit of the front-end stage operation for the case: $u_{\rm ga} > u_{\rm gb} > u_{\rm gc}$.

largest AC line-to-line voltages are deliberately switched to the output of the back-end semiconductor bridge and a cascading low-pass filtering (L_{oi} and $C_{\rm o}$) in order to regulate the output voltage $u_{\rm o}$. Correspondingly, the output voltage can ideally be adjusted to values starting from zero to:

$$u_o \le \sqrt{\frac{3}{2}} u_{{\rm g},l-l,{\rm rms}} \tag{1}$$

where, $u_{{\rm g},l-l,{\rm rms}}$ is the grid line-to-line RMS voltage.

A. System Operation of Two-Phase Clamped DPWM in Front-End AC-DC Stage

For the DPWM strategy studied in this work, two-phases are always clamped at each switching sequence, as a consequence, the DC-link voltage $u_{\rm pn}$ will be varied and be defined by two AC voltages with the largest magnitudes:

$$u_{\rm pn} = u_{\rm pos} - u_{\rm neg}. \tag{2}$$

where, $u_{\rm pos} = \max\{u_{\rm ga}, u_{\rm gb}, u_{\rm gc}\}$ is the maximum grid voltage and $u_{\rm neg} = \min\{u_{\rm ga}, u_{\rm gb}, u_{\rm gc}\}$ is the minimum one.

The operation of the back-end circuit impresses constant power $P_{\rm o}$ which will result in the demand of a current, I_x, varying in the opposite phase to the six-pulse rectifier voltage at the output of the front-end circuit or $u_{\rm pn}$:

$$\overline{I}_{\rm x} = \frac{P_{\rm o}}{u_{\rm pn}} = k_{\rm x}\frac{P_{\rm o}}{u_{\rm o}} = k_{\rm x} I_{\rm o}. \tag{3}$$

where $k_{\rm x}$ represents the relative on-time of the back-end Buck converter switch S_{ip} given by:

$$k_{\rm x} = \frac{u_{\rm o}}{u_{\rm pos} - u_{\rm neg}} = \frac{u_{\rm o}}{u_{\rm pn}}. \tag{4}$$

In the three-wire system, sinusoidal shape of all AC grid currents will be guaranteed by the overlaying of the circulating I_x with the current controlled by the switched phase-leg of the front-end circuit which has the lowest instant absolute voltage. Taking the condition that the grid voltage interval $[u_{\rm ga} > u_{\rm gb} > u_{\rm gc}]$ as an example, the equivalent circuit of the studied system is depicted in Fig. 2, where the voltage drop across the grid inductors is omitted and $S_{\rm bp}$ and $S_{\rm bn}$ are controlled to generate the required instant average current, i.e., $\overline{I}_{\rm bp}$ and $\overline{I}_{\rm bn}$. Assuming that the EV charging system operates as a symmetric three-phase load of phase conductance G to the grid, the value of the current to be controlled at phase b can be written as:

$$i_{\rm b} = G u_{\rm gb}. \tag{5}$$

If the voltage at the terminal b is formed according to the relative on-time of the switch $S_{\rm bp}$ as $k_{\rm y}$, it will result in:

$$\begin{aligned} u_{\rm bn} &= u_{\rm bN} + u_{\rm Nn} = -u_{\rm aN} - u_{\rm cN} - u_{\rm cN} = -u_{\rm pos} - 2u_{\rm neg} \\ &= k_{\rm y}(u_{\rm pos} - u_{\rm neg}) \end{aligned} \tag{6}$$

$$k_{\rm y} = \frac{-u_{\rm pos} - 2u_{\rm neg}}{u_{\rm pos} - u_{\rm neg}} = \frac{u_{\rm bN} - u_{\rm cN}}{u_{\rm pn}} = \frac{u_{\rm bc}}{u_{ac}} \tag{7}$$

By controlling the on-state of $S_{\rm bp}$ with a relative time $k_{\rm y}$, a sinusoidal current $i_{\rm a}$ will result of the overlay between I_x and the instant average current in $S_{\rm bp}$, $\overline{I}_{\rm bp}$, as followings:

$$\overline{I}_{\rm bp} = k_{\rm y} i_{\rm b} = G u_{\rm gb}\frac{u_{\rm bc}}{u_{\rm ac}} \tag{8}$$

$$\overline{I}_{\rm x} = \frac{P_{\rm o}}{u_{\rm ac}} = \frac{i_{\rm a}u_{\rm ac} + i_{\rm b}u_{\rm bc}}{u_{\rm ac}} = G\frac{u_{\rm ga}u_{\rm ac} + u_{\rm gb}u_{\rm bc}}{u_{\rm ac}} \tag{9}$$

$$i_{\rm a} = \overline{I}_{\rm x} - \overline{I}_{\rm bp} = G\left(\frac{u_{\rm ga}u_{\rm ac} + u_{\rm gb}u_{\rm bc}}{u_{\rm ac}} - \frac{u_{\rm gb}u_{\rm bc}}{u_{\rm ac}}\right) = G u_{\rm ga} \tag{10}$$

Additionally, a sinusoidal current $i_{\rm c}$ will result of the overlay between I_x and the instant average current in $S_{\rm bn}$, $\overline{I}_{\rm bn}$:

$$\overline{I}_{\rm bn} = (1 - k_{\rm y}) i_{\rm b} = G u_{\rm gb}(1 - \frac{u_{\rm bc}}{u_{\rm ac}}) = G u_{\rm gb}\frac{u_{\rm ab}}{u_{\rm ac}} \tag{11}$$

$$\begin{aligned} i_{\rm c} &= -\overline{I}_{\rm x} - \overline{I}_{\rm bn} = G\left(-\frac{u_{\rm ga}u_{\rm ac} + u_{\rm gb}u_{\rm bc}}{u_{\rm ac}} - \frac{u_{\rm ab}u_{\rm gb}}{u_{\rm ac}}\right) \\ &= G\frac{(u_{\rm gb} + u_{\rm gc})u_{\rm ac} - u_{\rm gb}u_{\rm bc} - u_{\rm gb}u_{\rm ab}}{u_{\rm ac}} = G u_{\rm gc} \end{aligned} \tag{12}$$

Therefore, sinusoidal shape of all grid currents for the interval $[u_{\rm ga} > u_{\rm gb} > u_{\rm gc}]$ has been proven.

Via this method, a sinusoidal current input and the controlled output voltage for all grid intervals can be achieved. Two phases with the maximum magnitude grid voltage are clamped, while only the one with the lowest instant absolute voltage is modulated with a relative on-time $k_{\rm y}$, together with the back-end circuit constantly modulated with the on-time $k_{\rm x}$. Assuming a high power factor operation, only the phase-leg with the lowest absolute value is switched at each time, leading to an optimum clamping strategy where the switching losses of the front-end converter can be the lowest compared to any other known DPWM strategies.

B. System Operation Variable Frequency ZVS Strategies in Back-End DC-DC Stage

The simplified topology of the back-end interleaved DC-DC circuit with one phase-leg, i.e., phase-leg 1, is given in Fig. 3(a). The typical current and voltage waveforms and of the ZVS operation are presented in Fig. 3(b), where $t_{\rm p,on}$ and $t_{\rm p,off}$ are the turn-on and turn-off time of the upper switch $S_{1\rm p}$; $T_{\rm s}$ is the switching period; $\Delta i_{\rm o1}$ and $i_{\rm o1,avg}$ are the current ripple and the average current value of $i_{\rm o1}$, respectively; $u_{\rm ds,p}$ is the drain to

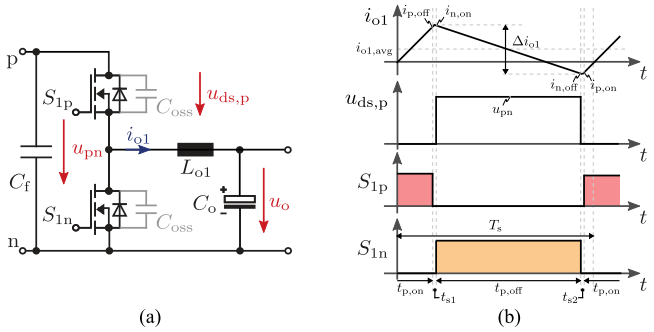

Fig. 3. Circuit cell of the PWM interleaved DC-DC circuit, (a) Circuit phase-leg 1, (b) current and voltage waveforms for TCM-ZVS or B-ZVS.

source voltage of S_{1pn}, C_{oss} is the equivalent output capacitance of the switches. After the turn-off command the C_{oss} of the upper/lower switch is charged from 0 to u_{pn}, while the other device within the half-bridge which will be turned-on next is discharged from u_{pn} to 0 before the switching transition.

As shown in Fig. 3, when the inductor current i_{o1} reaches $i_{p,off}$, S_{1p} is turned off. Then, the i_{o1} resonates from $i_{p,off}$ to the S_{1n} turn-on current $i_{n,on}$, during the first dead-time t_{s1}. After S_{1n} is turned on, the i_{o1} linearly decreases from $i_{n,on}$ to $i_{n,off}$ during the $t_{p,off}$. After S_{1n} is turned off, the i_{o1} is resonant again from $i_{n,off}$ to the S_{1p} turn-on current $i_{p,on}$, and the drain to source voltage $u_{ds,p}$ is resonant from u_{pn} to 0 during the second dead-time t_{s2}. After the conduction of its body-diode, S_{1p} can be turned on with ZVS. To achieve ZVS turn-on, the S_{1n} turn-off current $i_{n,off}$ should be adjusted as following [24]:

$$i_{n,off} \le \begin{cases} -\sqrt{\frac{2C_{oss}u_{pn}}{L_{o1}}(2u_o - u_{pn})}, & \text{if } 2u_o \ge u_{pn} \\ 0, & \text{if } 2u_o < u_{pn} \end{cases} \quad (13)$$

where the equivalent capacitance C_{oss} is calculated by:

$$C_{oss} = \frac{1}{u_{pn}} \int_0^{u_{pn}} C_{ds}(u_{ds}) \mathrm{d}u_{ds}. \quad (14)$$

Thereafter, the current ripple Δi_{o1} can be expressed as:

$$\Delta i_{o1} = \frac{(1-d)u_o}{L_{o1} f_{sb}} \quad (15)$$

where, $d = u_o/u_{pn}$ is the back-end circuit voltage conversion ratio. $i_{n,off}$ can be written as the function of Δi_{o1}:

$$i_{n,off} = i_{o1,avg} - \frac{\Delta i_{o1}}{2} = i_{o1,avg} - \frac{(1-d)u_o}{2L_{o1} f_{sb}} \quad (16)$$

where f_{sb} is the switching frequency of the DC-DC converter. It can be seen that both Δi_{o1} and $i_{n,off}$ are determined by f_{sb}. Therefore, due to the constant change in u_{pn}, ZVS operation can be realized with a variable switching frequency controller.

1) TCM-ZVS: The switching frequency f_{sb} for the back-end interleaved Buck DC-DC circuit in TCM-ZVS operation is calculated on the run based on the variable frequency control as:

$$f_{sb} = \frac{(1-d)u_o}{2L_o(i_{avg} + |i_{n,off}|)} \quad (17)$$

TABLE I
MAIN MODULATION FUNCTIONS FOR THE STUDIED DC-TYPE EV CHARGER

Sector	k_y	k_x or m_{Buck}	m_a	m_b	m_c
1	$u^*_{bc}/\,u^*_{ac}$	$u^*_o/\,u^*_{ac}$	1	k_y	0
2	$u^*_{ac}/\,u^*_{bc}$	$u^*_o/\,u^*_{bc}$	k_y	1	0
3	$u^*_{ca}/\,u^*_{ba}$	$u^*_o/\,u^*_{ba}$	0	1	k_y
4	$u^*_{ba}/\,u^*_{ca}$	$u^*_o/\,u^*_{ca}$	0	k_y	1
5	$u^*_{ab}/\,u^*_{cb}$	$u^*_o/\,u^*_{cb}$	k_y	0	1
6	$u^*_{cb}/\,u^*_{ab}$	$u^*_o/\,u^*_{ab}$	1	0	k_y

where i_{avg} can be obtained from the current measurement sensor for i_{o123}. The TCM-ZVS strategy implements the change in f_{sb} to keep $i_{n,off}$ and Δi_{o123} constant for the whole range of u_{pn}.

2) B-Zvs: Since the DC-link voltage u_{pn} is variable with the two-phase clamped DPWM strategy in the front-end AC-DC converter, the f_{sb} for TCM-ZVS should be updated in every calculation cycle. To simplify the computation, B-ZVS is introduced also with the variable frequency control as:

$$d_{max} = \frac{u_o}{u_{pn,min}} = \frac{u_o}{\sqrt{\frac{3}{2}} u_{g,l-l,rms}} \quad (18)$$

$$f_{sb,min} = \frac{(1-d_{max})u_o}{2L_o(i_{avg} + |i_{n,off}|)} \quad (19)$$

It can be found that the B-ZVS method sets a f_{sb} which guarantees that for the minimum u_{pn} the condition given in (13) is satisfied, and the ZVS operation can be achieved naturally with higher u_{pn} operating points. With B-ZVS strategy, f_{sb} do not need to change under a constant output power.

C. Overall Coupled Control Strategy With the Proposed Hybrid Modulation

A possible implementation of a feedback control and PWM modulation strategy for the studied EV charging system is shown in Fig. 4. This control scheme includes an outer DC voltage loop for u_o, which together with the information of the AC voltages u_{gabc} generates the AC current references i^*_{abc}. This voltage control loop also set the reference for the inductor currents i_{o123} across the interleaved Buck-converters. Since a lager voltage ripple than other normal PWM strategies [25] in the DC-link is allowed via this coupled modulation, a DC-link capacitor with low energy storage capability can be used. The modulation functions for the two-phase clamped DPWM strategy in both front- and back-end stages ensuring high-power-factor operation, m_a, m_b, m_c and m_{Buck}, are synthesized from the six grid voltage sectors, as defined in Fig. 5, and the voltage reference, $u^*_{ab}/\,u^*_{bc}/\,u^*_{ca}/\,u^*_{ba}/\,u^*_{cb}/\,u^*_{ac}/\,u^*_o$, as described in Table I. The variables m_1, m_2, m_3 are the modulation functions for the interleaved phase legs 1, 2 and 3 in the back-end DC-DC stage, which are the sum of m_{Buck} and the output of the DC current controllers $G_{i_{o123}}$. It can be found that in each sector two phase-legs are always clamped, either 1 or 0.

The switching frequency for the back-end interleaved DC-DC stage is calculated on the run based on the presented TCM-ZVS

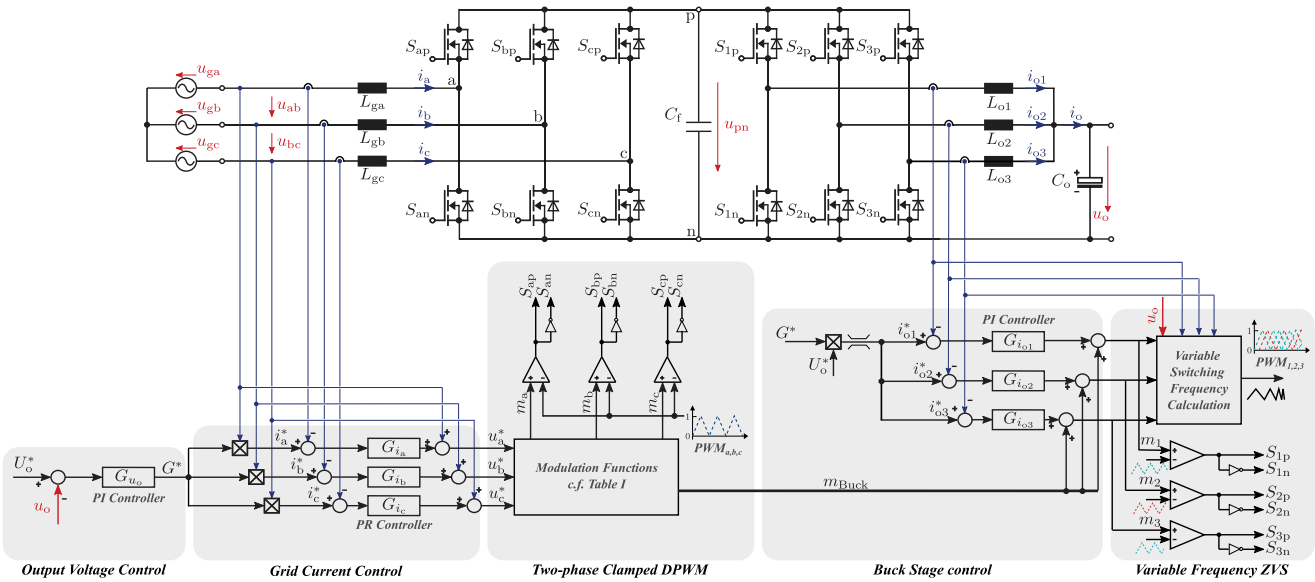

Fig. 4. Feedback control architecture of the DC-type EV charger.

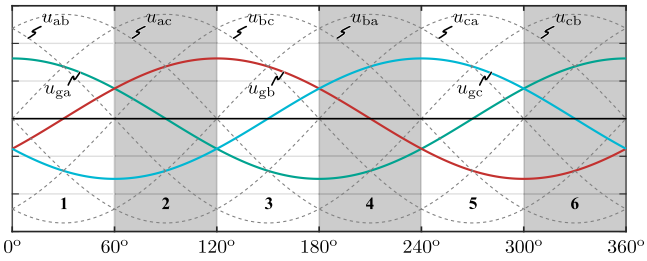

Fig. 5. Grid voltage sectors defined by different relations of the instantaneous values of the grid phase voltages.

in (17) and B-ZVS in (19), where $d = m_1 = m_2 = m_3$ from the modulation function.

TABLE II
SPECIFICATIONS FOR THE PROTOTYPE

Variables	Parameters	Value
P_o	Rated output power	5 kW
$u_\mathrm{g,rms}$	Grid voltage	220 V
ω	Grid angular frequency	$2\pi \times 50$ rad/s
u_dc	DC voltage	400 V
L_g	Grid inductance	720 μH
L_o	Storage filter inductance	240 μH
C_o	Output capacitance	80 μF
C_f	DC-link capacitance	5 μF
$S_\mathrm{abc,p/n}$	Active switch for front-end	C3M0120090J
$S_\mathrm{123,p/n}$	Active switch for back-end	C3M0120090J

III. SEMICONDUCTOR STRESSES

To provide a general guideline for the design of the studied DC-type EV charger depicted in Fig. 1, the stresses of the active switches of both the front- and back-end converters are calculated analytically, which is based on SMD Silicon Carbide (SiC) MOSFETs (900 V, 120 mΩ, C3M0120090 J from CREE [34]). It is assumed: a sinusoidal AC current shape; a constant DC current i_o; hard-switching in the front-end stage; unity power factor; no low-frequency voltage drop across the input filter inductors; and a switching frequency f_s being much higher than the grid frequency f_g, i.e., $f_\mathrm{s} \gg f_\mathrm{g}$. The specifications of the converter are given in Table II. It is noted that to make the temperatures on the case of the package and PCB board within safe operating range at full power, three units in parallel are used.

There are four different hybrid modulation solutions for the presented two-stage AC-DC converter benchmarked in this section, which are defined as follows:

1) **PWM1**: Traditional SVPWM method is applied in the front-end stage, and the fixed f_sb is used in the back-end stage.
2) **PWM2**: Two-phase clamped DPWM method is applied in the front-end stage, and the fixed f_sb is used in the back-end stage.
3) **PWM3**: Two-phase clamped DPWM method is applied in the front-end stage, and the B-ZVS strategy is used in the back-end stage.
4) **PWM4**: Two-phase clamped DPWM method is applied in the front-end stage, and the TCM-ZVS strategy is used in the back-end stage.

For a fair comparison, with the PWM1 case, the u_pn should be controlled to be $\sqrt{2}u_{\mathrm{g},l-l,\mathrm{rms}} \approx 539$ V to get a maximum modulation index, i.e., 1.15, in the AC-DC converter. For all modulation solutions, the switching frequency for the front-end stage is the same as the fixed f_sb used in the back-end stage as PWM1 and PWM2, which is defined by the average switching frequency $f_\mathrm{sb,avg}$ with TCM-ZVS at the full output power:

$$f_\mathrm{sb,avg} = \int_0^{\frac{\pi}{6}} \frac{(1-d(\omega t))\,u_\mathrm{o}}{2L_\mathrm{o}(i_\mathrm{avg}+|i_\mathrm{n,off}|)}\mathrm{d}\omega t \approx 36\,\mathrm{kHz} \qquad (20)$$

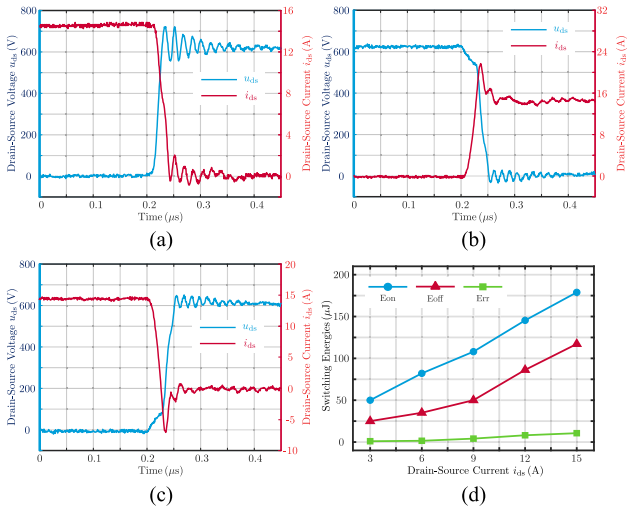

Fig. 6. Measured switching characteristics of one phase leg at $u_{ds} = U_b = 600$ V and gate resistance $R_g = 10\,\Omega$ (a) turn-off transient (b) turn-on transient (c) anti-parallel diode reverse recovery transient (d) relationship between switching energy and load current.

TABLE III
FITTED SWITCHING LOSS COEFFICIENTS FOR ONE SIC MOSFET (C3M0120090 J) OPERATED AT $u_{pn} = 600$ V, VALID FOR $E_{sw}(I_{sw}) = a + b|I_{sw}| + c|I_{sw}|^2$

Coefficient	Turn-on Energy ($E_{on} + E_{rr}$)	Turn-off Energy (E_{off})
a in μJ	23.71	23.58
b in μJ/A	8.75	-1.17
c in μJ/A^2	0.16	0.50

A. Switching Losses

For the analytical calculation of switching losses, the following general equation can be used:

$$P_s = \frac{1}{2\pi}\int_0^{2\pi} f_s(\omega t) E_{sw}(u_{pn,sw}, I(\omega t))\mathrm{d}\omega t. \tag{21}$$

where E_{sw} represents the device switching energy as function of the switched voltage $u_{pn,sw}$ and current I_{sw}. $E_{sw}(u_{pn,sw})$ can be considered linear, and the local switching losses of the semiconductor can be described with a quadratic loss function of $E_{sw}(I_{sw}) = a + b|I_{sw}| + c|I_{sw}|^2$[35]. With the selected switching device, the considered fittings coefficients are based on the experimental double pulse test results as shown in Fig. 6 and listed in Table III.

The analysis of the switching losses for the front-end stage can be found in [36]. Herein, if the back-end stage works under the TCM-ZVS operation, the ripple current flowing through L_{oi} should be constant and equal to:

$$\Delta i_{o,pp} = 2\,(i_{avg} + |i_{n,off}|) \tag{22}$$

Based on the specifications presented in Table II, the maximum equivalent $C_{oss} \approx 266$ pF (C3M0120090 J, three in parallel), and thus the maximum value of $|i_{n,off}|$ based on (13) is approximately 587 mA. To ensure enough margin, $|i_{n,off}| = 1$ A is selected. Thereafter, the turn-off switching current can be expressed as:

$$I_{sw_{off,zvs}} = i_{avg} + (i_{avg} + |i_{n,off}|) \tag{23}$$

With TCM-ZVS turn-on the switching losses per device for the back-end DC-DC converter is:

$$P_s = \frac{1}{2\pi U_b}\int_0^{2\pi} f_{sb}(\omega t) u_{pn}(\omega t) E_{sw_{off}}(I_{sw_{off,zvs}}(\omega t))\mathrm{d}\omega t. \tag{24}$$

With B-ZVS operation the term $f_{sb}(\omega t)$ in (24) is replaced by $f_{sb,min}$ in (19) which is variable mainly as function of i_{avg} and u_o.

If the back-end stage is operated under hard-switching, the current flowing through L_{oi} is expressed as (15), and the turn-on and turn-off switching current are:

$$I_{sw_{on,h}} = i_{avg} - \frac{\Delta i_{o,pp}}{2} \tag{25}$$

$$I_{sw_{off,h}} = i_{avg} + \frac{\Delta i_{o,pp}}{2} \tag{26}$$

Both the turn-on and turn-off switching losses should be considered as:

$$P_s = \frac{f_{sb}}{2\pi U_b}\int_0^{2\pi} u_{pn}(\omega t) E_{sw_{on}}(I_{sw_{on,h}}(\omega t)) + u_{pn}(\omega t) E_{sw_{off}}(I_{sw_{off,h}}(\omega t))\mathrm{d}\omega t. \tag{27}$$

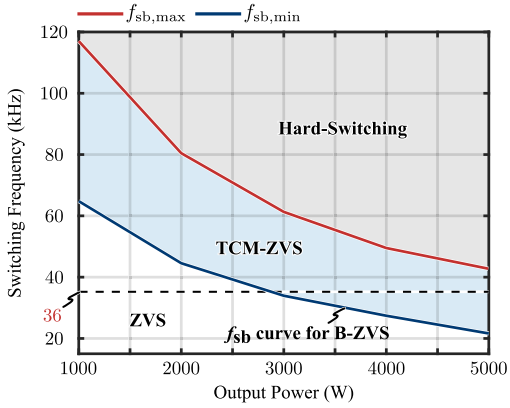

Fig. 7. f_{sb} operating ranges and limits at $u_o = 400$ V.

Fig. 7 shows the variation of switching frequency of the back-end stage f_{sb} with different output power at $u_o = 400$ V. f_{sb} for TCM-ZVS varies between its upper and lower limits, $f_{sb,max}$ and $f_{sb,min}$, according to the variation of u_{pn}. If the f_{sb} is lower than $f_{sb,min}$ (cf. (19)), the back-end stage is always operating at ZVS turn on action due to the fact the turn-off current will always be lower than the required value, while, if the f_{sb} is higher than $f_{sb,max}$, then it is always operating at hard-switching. For the PWM1 case, the minimum f_{sb} to allow ZVS operation in the back-end stage under $u_{pn} = 539$ V and full power 5 kW is 41.2 kHz $> f_{sb,selected} = 36$ kHz. Therefore, ZVS characteristics in the back-end stage can be achieved with PWM1 as well. For the PWM2 case, due to the variable u_{pn}, ZVS operation for the back-end stage will be lost under some operating points with

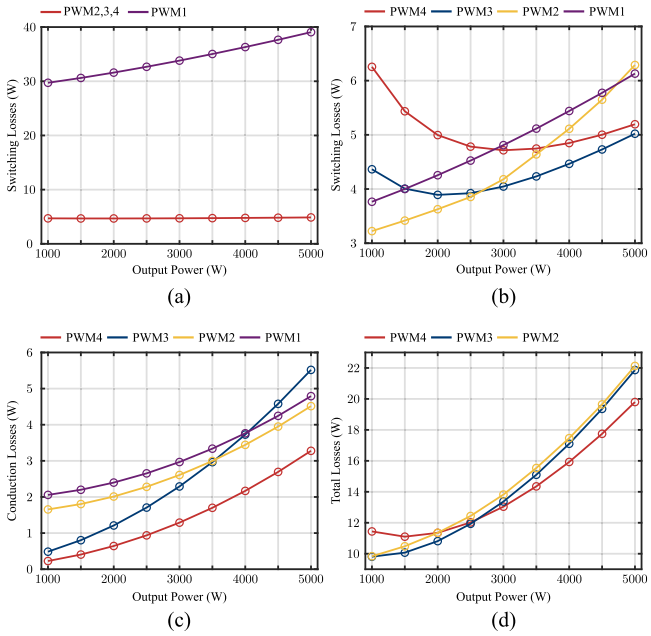

Fig. 8. Calculated semiconductor losses comparison at $u_{\rm o} = 400$ V, (a) switching losses in front-end stage, (b) switching losses in back-end stage, (c) conduction losses in back-end stage, (d) total losses of the two-stage converter.

low $u_{\rm pn}$, e.g., as shown in Fig. 7 when $P_{\rm o} > 3\,{\rm kW}$. The comparison of switching losses in the front-end converter with different modulation solutions is shown in Fig. 8(a). It is clear that the switching losses can be reduced remarkably by the two-phase clamped DPWM compared to traditional SVPWM with constant DC-link voltage, i.e., nearly 87.5% switching losses reduction. The comparison of switching losses in the back-end converter with different modulation solutions is presented in Fig. 8(b). It can be found that at low output power level, the switching losses of the two ZVS strategies in PWM3 and PWM4 are higher than the fixed $f_{\rm sb}$ in PWM1 and PWM2 due to the considerable increment of $f_{\rm sb}$, which can reach more than 100 kHz. However, with the output power increasing, the switching losses of the ZVS strategies will be reduced considerably. The B-ZVS in PWM3 has the best performance in the switching losses at high output power, and the difference between B-ZVS and TCM-ZVS reduces with the increment of power. At high output power, PWM2 may lose ZVS operation due to the variable DC-link voltage, and thus the switching losses achieved by PWM2 is slightly higher than that by PWM1.

B. Conduction Losses

For unipolar power semiconductors, i.e. SiC MOSFET, assuming that the device channel is used also for reverse conduction, conduction losses depend on the RMS current flowing through the switches, $I_{\rm rms}$, and the drain-source on-state resistance, $R_{\rm ds}$:

$$P_{\rm c} = R_{\rm ds} I_{\rm rms}^2. \tag{28}$$

Considering a pure sinusoidal phase current:

$$i_{\rm g}(\omega t) = I_{\rm g} \cos(\omega t), \tag{29}$$

where $I_{\rm g} = \sqrt{2} P_{\rm o}/(3u_{\rm g,rms})$ is the peak AC line current, and ω is the grid angular frequency.

The RMS currents across $S_{\rm abc,p/n}$ and $S_{\rm 123,p/n}$ can be calculated solving:

$$I_{S_{\rm abc,p/n,rms}} = \sqrt{\frac{1}{2\pi}\int_0^{2\pi} i_{\rm g}^2(\omega t) k_{\rm y}(\omega t) {\rm d}\omega {\rm t}} = \frac{I_{\rm g}}{2} \tag{30}$$

$$I_{S_{\rm 123,p,rms}} = \sqrt{\frac{6}{\pi}\int_0^{\frac{\pi}{6}} d(\omega t)(i_{oi,\rm avg}^2 + \frac{\Delta i_{\rm o1}^2(\omega t)}{12}){\rm d}\omega {\rm t}} \tag{31}$$

$$I_{S_{\rm 123,n,rms}} = \sqrt{\frac{6}{\pi}\int_0^{\frac{\pi}{6}} (1-d(\omega t))(i_{oi,\rm avg}^2 + \frac{\Delta i_{\rm o1}^2(\omega t)}{12}){\rm d}\omega {\rm t}} \tag{32}$$

where,

$$\Delta i_{oi}(\omega t) = \begin{cases} (1-d(\omega t))\dfrac{u_{\rm o}}{L_{\rm o} f_{\rm sb}}, & \text{PWM1-3} \\ 2(i_{oi,\rm avg} + |i_{\rm n,off}|), & \text{PWM4} \end{cases} \tag{33}$$

Since $I_{\rm g}$ for different modulation solutions are the same, there is no obvious difference of conduction losses observed in the front-end stage. The comparison of conduction losses in the back-end stage is given in Fig. 8(c). It can be seen that the TCM-ZVS in PWM4 has the lowest conduction losses performance because of the lower equivalent Δi_{oi}, and with the power increased, the conduction losses obtained by B-ZVS in PWM3 get worse because of the lower operating $f_{\rm sb}$ and consequent higher Δi_{oi}, especially at high power.

The total losses comparison among the different operating strategies is shown in Fig. 8(d). Due to the fact that there is a large loss difference between PWM1 and other PWM solutions, the total losses achieved by PWM1 is not included in Fig. 8(d). Although the performance of B-ZVS in the switching losses is the best for most operating range, its conduction losses is the worst for high output power. Thus, the total losses improved by the B-ZVS in PWM3 is limited relative to that by PWM2 with fixed switching frequency. It can be found that the studied TCM-ZVS could provide the optimal solution of losses reduction at high power/output current, which is the normal operating mode in DC-type EV chargers.

Note that according to Fig. 7 at $P_{\rm o} < 3$ kW all four operation cases have ZVS turn-on characteristic in the back-end stage. The switching losses reduction for all modulation solutions with two-phase clamped DPWM is much better than that with traditional SVPWM. Due to the non-optimum ZVS turn-on for the B-ZVS in PWM3 and the fixed $f_{\rm sb}$ in PWM2, which will yield to a higher Δi_{oi} than that for the TCM-ZVS method in PWM4, the conduction losses across the MOSFETs will be increased. Nevertheless, the complexity of the implementation of the TCM-ZVS in PWM4 is higher than that for the other methods, because the variable switching frequency must follow both $i_{\rm avg}$, $u_{\rm o}$, and $u_{\rm pn}$ and should be ideally updated at every switching cycle, while B-ZVS in PWM3 mostly change with $i_{\rm avg}$ when the output voltage $u_{\rm o}$ is constant.

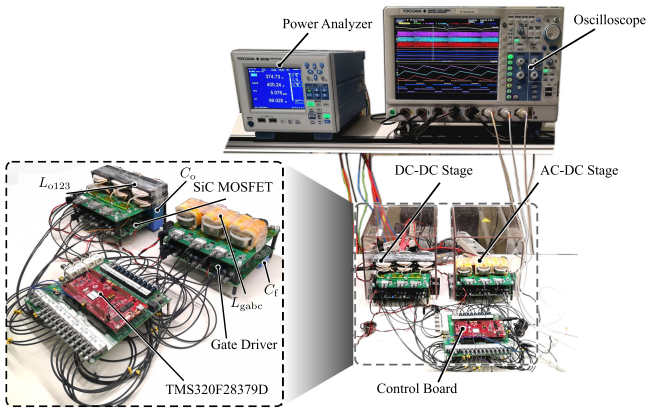

Fig. 9. Experimental setup.

IV. Simulation and Experimental Evaluation

To validate the effectiveness of the utilization of the proposed hybrid modulation, simulation and experimental tests are conducted and benchmarked with different modulation solutions, i.e., PWM1-4 as described in the previous section. A PLECS based simulation is carried out first to verify the effectiveness of the proposed method. Then, the studied strategies is operated on a digital-controlled hardware platform with digital signal processor (DSP) from the Texas Instruments, C2000 TMS320F28379D, as shown in Fig. 9. The specifications of the prototype are the same as listed in Table II. All of the experimental waveforms are recorded by the oscilloscope YOKOGAYA DLM4058, and the current total harmonic distortions (THD) and power conversion efficiency are tested by the power analyser YOKOGAYA WT500.

Fig. 10 shows the simulation results of the steady-state operation of the studied DC-type EV charger operating with the two-phase clamped DPWM strategy in the front-end stage and TCM-ZVS in the back-end stage at $u_{\rm o} = 400\,{\rm V}$, $P_{\rm o} = 5\,{\rm kW}$. It can be seen that two-thirds of the switching signal is clamped, while sinusoidal input AC currents are obtained in the front-end stage. The current ripples of $i_{\rm o1}$, $i_{\rm o2}$, and $i_{\rm o3}$ keep constant when the duty cycle of the back-end stage is changing, and the switching signals are interleaved. The effectiveness of the proposed method can be verified through the simulation results.

The main experimental results of the studied circuit operating with TCM-ZVS in the back-end circuit, i.e., PWM4, at 400 V and 5 kW are shown in Fig. 11. The experimental results demonstrate that the front-end AC currents $i_{\rm a}$, $i_{\rm b}$, and $i_{\rm c}$ can effectively follow the sinusoidal input AC voltages, while the current across the parallel back-end converter are well balanced, attesting the feasibility of the studied circuit and control method depicted in Fig. 4. It is clearly observed that in Fig. 11(a), at every moment, the switching signals for two phase-legs are always clamped, either at high (positive DC-rail) or low (negative DC-rail). Additionally, due to the high power factor operation only the phase-leg conducting the lowest current magnitude is switched which can reduce the switching losses of the front-end stage considerably. In Fig. 11(b), it can be seen that for the

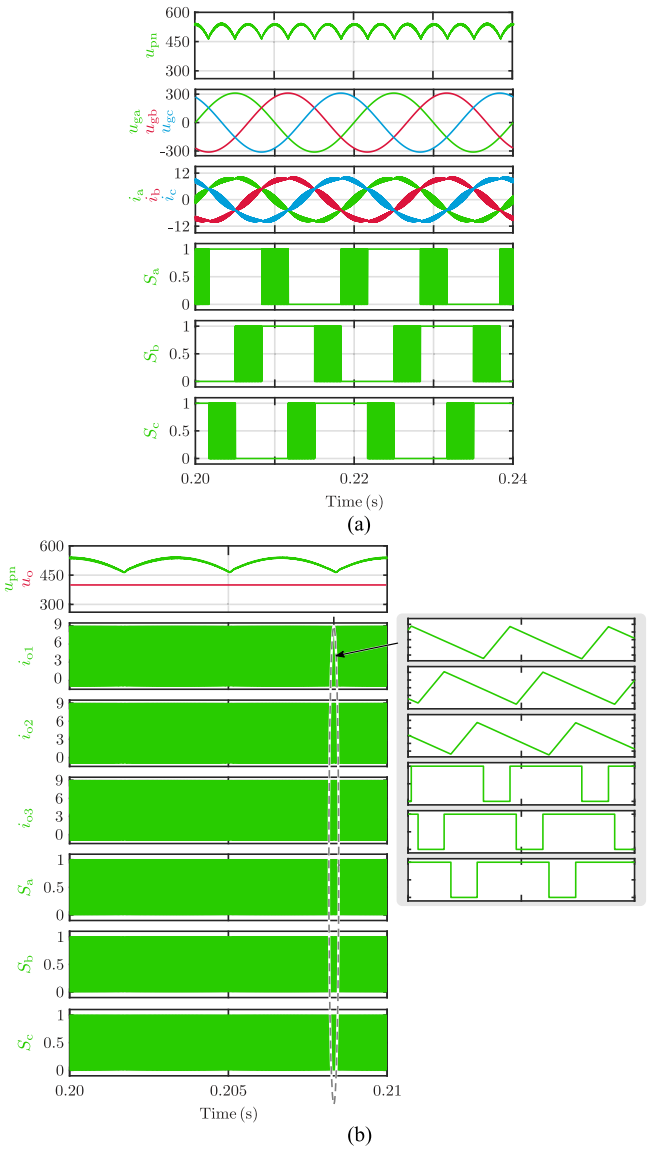

Fig. 10. Simulation results of the steady-state operation of the studied DC-type EV charger operating with the proposed hybrid modulation method, i.e., PWM4, at 400 V, 5 kW for (a) front-end and (b) back-end converter stages.

back-end circuit the current ripples of $i_{\rm o1}$, $i_{\rm o2}$, and $i_{\rm o3}$ are constant because $f_{\rm sb}$ was dynamically adjusted according to (17), and note that there is a symmetric phase-shift between the three paralleled half-bridge legs, which verifies that the variable frequency TCM-ZVS strategy was effectively implemented. The experimental results match well with the simulation results presented in Fig. 10. The system operation result of the two-stage converter with conventional strategy, i.e., PWM1, is presented in Fig. 12. Different from the proposed hybrid solution, the switches of the front-end stage is switched every time and the DC-link voltage is constant.

Fig. 13 shows the experimental results of the switching transients of the back-end stage at 5 kW with both fixed $f_{\rm sb}$ in PWM2 and TCM-ZVS in PWM4. With the fixed $f_{\rm sb}$ in PWM2, the current ripple across the output inductors varies following the changes of $u_{\rm pn}$. If $u_{\rm pn}$ takes the minimum value, $\Delta i_{\rm o,pp}$ will

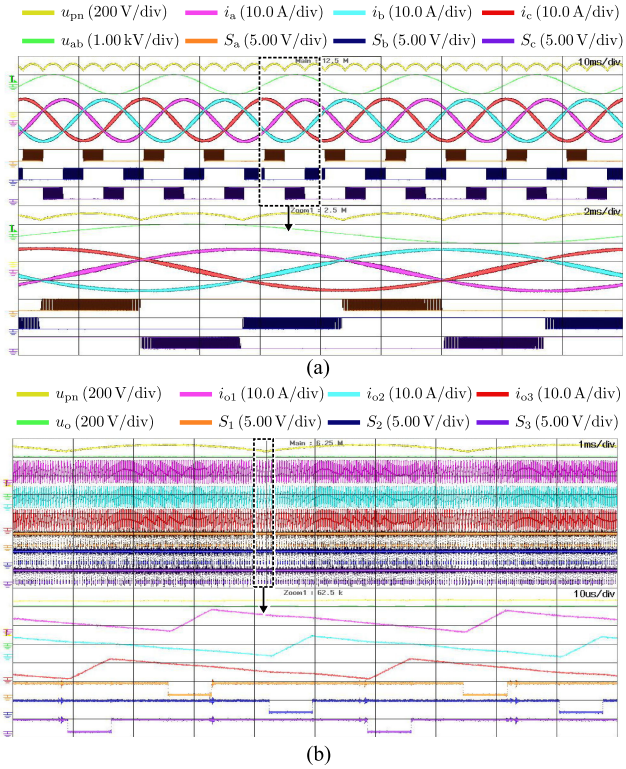

Fig. 11. Experimental results of the studied circuit with the proposed hybrid modulation method, i.e., PWM4, at 400 V, 5 kW for (a) front-end and (b) back-end converter stages.

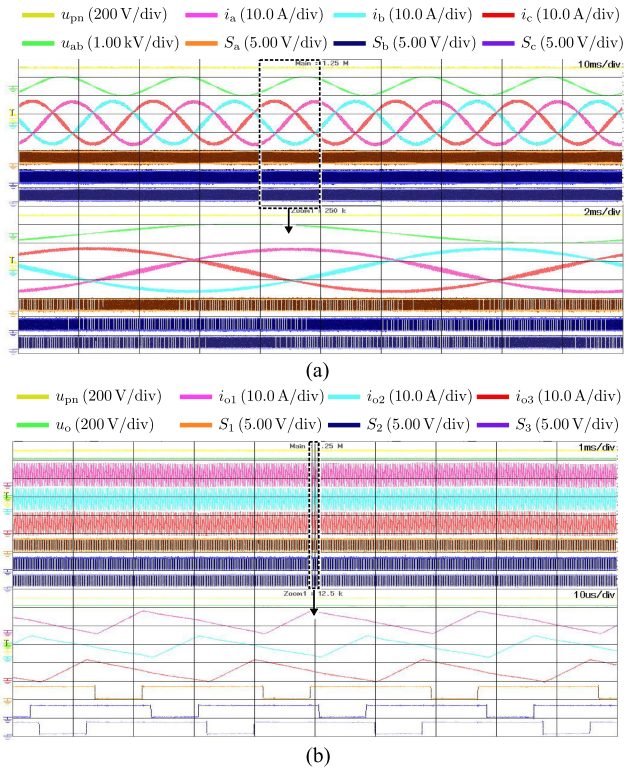

Fig. 12. Experimental results of the studied circuit with traditional modulation method, i.e., PWM1, at 400 V, 5 kW for (a) front-end and (b) back-end converter stages.

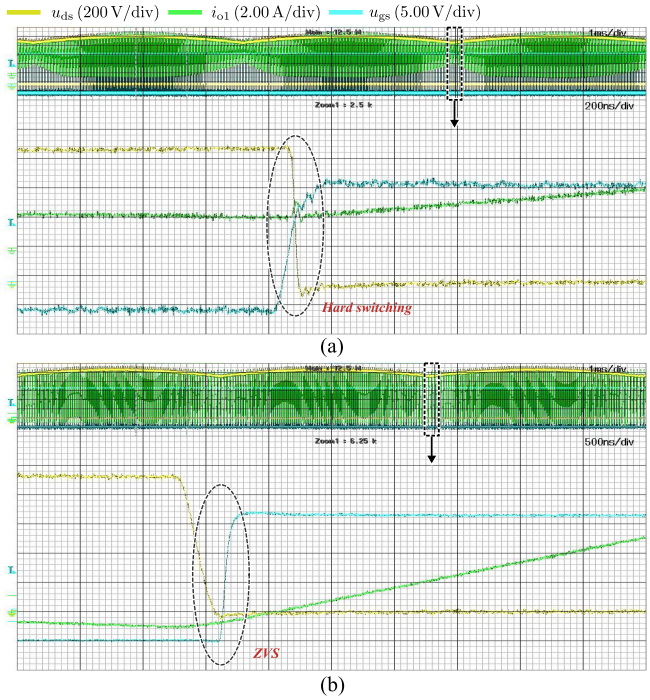

Fig. 13. Experimental results of the switching transients in the back-end stage at 5 kW for (a) fixed f_{sb} in PWM2, (b) TCM-ZVS in PWM4.

also reach its minimal value. The turn-on current is greater than 0, and thus the back-end stage is operating at hard-switching mode, which can be clearly observed in the zoom function of the highlighted section of Fig. 13(a). On the other hand, with the TCM-ZVS strategy in PWM4, the turn-on current is nearly constant at -1 A, and ZVS turn-on operation can be achieved at the minimum u_{pn} point, as shown in the zoom function of the highlighted section of Fig. 13(b). The switching transients of the back-end stage with PWM1 and PWM3 is similar as that with PWM4.

Fig. 14 shows the measured total system power conversion efficiency among different modulation solutions implementing at the studied two-stage converter for different output power and DC output voltages. In Fig. 14(a), controlled by the implemented two-phase clamped DPWM (PWM2-4), a considerable improvement in the power efficiency of the converter can be achieved compared to the traditional SVPWM method (PWM1) as predicted by the theoretical analysis in Fig. 8(a). With the ZVS operation in the back-end stage, the power efficiency of the converter can be further improved by the proposed PWM3 and PWM4. The maximum efficiency obtained in the measurements is 99%, which is achieved at 400 V and 5 kW with the TCM-ZVS strategy in PWM4. Moreover, as discussed in the Section III, the efficiency improvement in the back-end stage achieved by B-ZVS is limited compared to the one achieved by the fixed f_{sb}. In Fig. 14(b), with a constant DC current, i.e., at $i_o = 12.5$ A, the power converter efficiency of the PWM4 is still better than the other modulations.

Fig. 15 shows the AC current THD among different modulation solutions with different output power and DC voltage. The

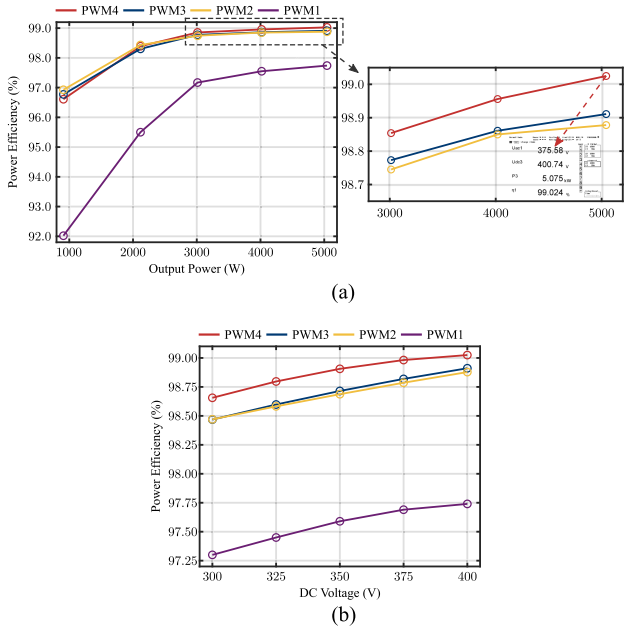

Fig. 14. Comparison between the measured power conversion efficiency for all analyzed PWM cases (a) output power at $u_o = 400\,\mathrm{V}$ (b) DC voltage at $i_o = 12.5\,\mathrm{A}$.

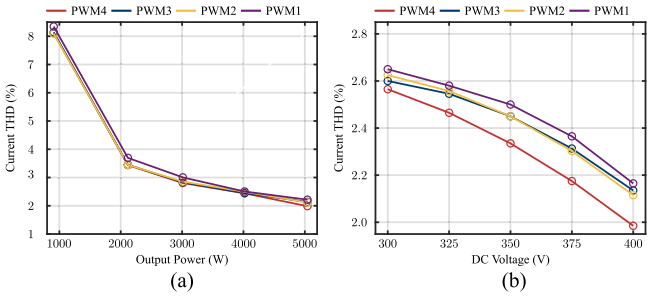

Fig. 15. Comparison between the AC Current THD for all analyzed PWM cases (a) output power at $u_o = 400\,\mathrm{V}$, (b) DC voltage at $i_o = 12.5\,\mathrm{A}$.

current THD in the front-end stage achieved by the two-phase clamped DPWM is better than that of the SVPWM. It is found that the variation of switching frequency in the back-end stage do not have a significant impact on the AC current THD. The current THD achieved with the TCM-ZVS in PWM4 is slightly lower, because the equivalent f_{sb} for TCM-ZVS is high and the harmonics coupled from the DC side to the AC side are relatively small, where the DC-link capacitance C_f and AC inductances L_{gabc} act as a low pass filter.

Fig. 16(a) shows the scaled down (50 kW to 5 kW) battery charging profile of a popular EV, i.e., the Nissan Leaf, from the state-of-charge (SoC) from 0% to 90%. Therein, the scaling down considers that the necessary 50 kW power is provided evenly by 10 parallel units of the designed prototype shown in Fig. 9. Fig. 16(b) presents the measured power efficiencies for the setup employing the four studied modulation strategies during the EV charging process. The proposed hybrid solution with TCM-ZVS provides the best efficiency performance as well over whole SoC range. Note that with the assumption that

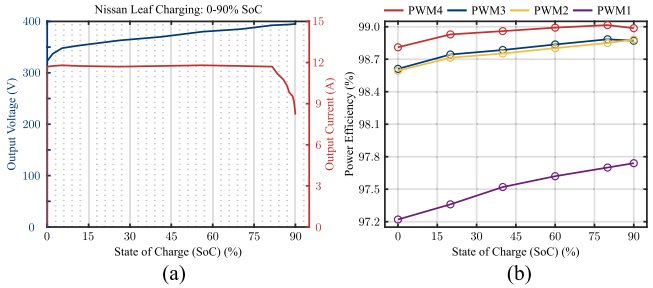

Fig. 16. (a) Equivalent Nissan Leaf charging profile for one 5 kW unit of ten paralleled converters and (b) measured power efficiency for all back-end converter studied modulation strategies. Note that all benchmarked strategies will feature ZVS turn-on for the whole charging profile.

TABLE IV
PERFORMANCE COMPARISON OF VARIOUS PWM METHODS

	PWM1	PWM2	PWM3	PWM4
ZVS range	full	low	full	full
Efficiency	low	high	high	very high
Complexity	low	moderate	high	very high

an even distribution of power occurs each paralleled converter will process P_o >3 kW for the whole charging range shown in Fig. 16(a). This will yield to ZVS turn-on of the back-end converter for most of the studied modulation strategies.

The advantages and disadvantages of the proposed method, PWM3 and PWM4, and the previous method, PWM1 and PWM2, are compared in Table IV. It can be found that except for PWM2, every PWM method has the feature of ZVS turn-on operation. The proposed methods, i.e., TCM-ZVS and B-ZVS strategies, can lead to a higher efficiency, but they will increase the complexity of the system, which needs to consume more computation power to get the required switching frequency.

All in all, the presented simulation and experimental results have shown that a remarkable reduction on power losses with the proposed hybrid modulation has been achieved in the studied DC-type EV charger system. This confirms the superiority of the proposed method when compared to the other analyzed strategies. Therefore, the validity and advantages of the proposed strategy are verified.

V. CONCLUSION

This work has evaluated a two-stage AC-DC power converter employing a new hybrid modulation strategy for DC-type EV chargers, where two-phase clamped DPWM strategy is implemented for the front-end AC-DC circuit and ZVS turn-on is safeguarded over a large operating range for the back-end DC-DC circuit. The high power factor operation of the system with two-phase clamped DPWM strategy is only possible when a low energy storage exists between the two cascaded converters, which makes the operation of both circuits highly coupled to each other. The principle of operation and implementation of the necessary synergetic control strategy for both converter stages have been explained in detail. The mathematical models of the semiconductor stresses have been described as well. It

was shown that the two-phase clamped DPWM method can achieve a remarkable switching losses reduction in the front-end stage compared to the traditional SVPWM method. Moreover, in an EV charging application the semiconductor losses of the TCM-ZVS in the back-end stage is superior to that achieved with B-ZVS and the fixed frequency operation. Simulation and experimental results have been used to verify the effectiveness and superiority of the proposed method. The 99% power conversion efficiency has been achieved at 400 V and 5 kW with the TCM-ZVS strategy in the back-end stage, which is 1.3% higher than the traditional solution.

REFERENCES

[1] V. Monteiro, J. G. Pinto, and J. L. Afonso, "Operation modes for the electric vehicle in smart grids and smart homes: Present and proposed modes," *IEEE Trans. Veh. Technol.*, vol. 65, no. 3, pp. 1007–1020, Mar. 2016.

[2] T. B. Soeiro and P. Bauer, "Fast DC-type electric vehicle charger based on a quasi-direct boost-buck rectifier," in *Proc. AEIT Int. Conf. Elect. Electron. Technol. Automot.*, 2019, pp. 1–6.

[3] T. B. Soeiro and P. Bauer, "Three-phase unidirectional quasi-single-stage delta-switch rectifier DC-DC buck converter," in *Proc. 45th Annu. Conf. IEEE Ind. Electron. Soc.*, vol. 1, 2019, pp. 3479–3484.

[4] E. Ucer *et al.*, "Analysis, design, and comparison of v2v chargers for flexible grid integration," *IEEE Trans. Ind. Appl.*, vol. 57, no. 4, pp. 4143–4154, Jul./Aug. 2021.

[5] I. Aghabali, J. Bauman, P. J. Kollmeyer, Y. Wang, B. Bilgin, and A. Emadi, "800-v electric vehicle powertrains: Review and analysis of benefits, challenges, and future trends," *IEEE Trans. Transport. Electrific.*, vol. 7, no. 3, pp. 927–948, Sep. 2021.

[6] D. Menzi, D. Bortis, and J. W. Kolar, "Three-phase two-phase-clamped boost-buck unity power factor rectifier employing novel variable DC link voltage input current control," in *Proc. IEEE Int. Power Electron. Appl. Conf. Expo.*, 2018, pp. 1–8.

[7] D. Menzi, D. Bortis, and J. W. Kolar, "A new bidirectional three-phase phase-modular boost-buck AC/Dc converter," in *Proc. IEEE Int. Power Electron. Appl. Conf. Expo.*, 2018, pp. 1–8.

[8] A. Khaligh and S. Dusmez, "Comprehensive topological analysis of conductive and inductive charging solutions for plug-in electric vehicles," *IEEE Trans. Veh. Technol.*, vol. 61, no. 8, pp. 3475–3489, Oct. 2012.

[9] D. Aggeler *et al.*, "Ultra-fast dc-charge infrastructures for ev-mobility and future smart grids," in *Proc. IEEE PES Innov. Smart Grid Technol. Conf. Europe*, 2010, pp. 1–8.

[10] M. Vasiladiotis and A. Rufer, "A modular multiport power electronic transformer with integrated split battery energy storage for versatile ultrafast EV charging stations," *IEEE Trans. Ind. Electron.*, vol. 62, no. 5, pp. 3213–3222, May 2015.

[11] H. N. de Melo, J. P. F. Trovão, P. G. Pereirinha, H. M. Jorge, and C. H. Antunes, "A controllable bidirectional battery charger for electric vehicles with vehicle-to-grid capability," *IEEE Trans. Veh. Technol.*, vol. 67, no. 1, pp. 114–123, Jan. 2018.

[12] V. Monteiro, J. C. Ferreira, A. A. Nogueiras Meléndez, C. Couto, and J. L. Afonso, "Experimental validation of a novel architecture based on a dual-stage converter for off-board fast battery chargers of electric vehicles," *IEEE Trans. Veh. Technol.*, vol. 67, no. 2, pp. 1000–1011, Feb. 2018.

[13] L. Wang, Z. Qin, T. Slangen, P. Bauer, and T. van Wijk, "Grid impact of electric vehicle fast charging stations: Trends, standards, issues and mitigation measures - an overview," *IEEE Open J. Power Electron.*, vol. 2, pp. 56–74, 2021, doi: 10.1109/OJPEL.2021.3054601.

[14] S.-W. Choi, S.-T. Oh, M.-W. Kim, I.-O. Lee, and J.-Y. Lee, "Interleaved isolated single-phase PFC converter module for three-phase EV charger," *IEEE Trans.Veh. Technol.*, vol. 69, no. 5, pp. 4957–4967, May 2020.

[15] J. W. Kolar and T. Friedli, "The essence of three-phase PFC rectifier systems-part I," *IEEE Trans. Power Electron.*, vol. 28, no. 1, pp. 176–198, Jan. 2013.

[16] T. Friedli, M. Hartmann, and J. W. Kolar, "The essence of three-phase PFC rectifier systems-part II," *IEEE Trans. Power Electron.*, vol. 29, no. 2, pp. 543–560, Feb. 2014.

[17] Y. Lee, A. Khaligh, and A. Emadi, "Advanced integrated bidirectional AC/DC and DC/DC converter for plug-in hybrid electric vehicles," *IEEE Trans. Veh. Technol.*, vol. 58, no. 8, pp. 3970–3980, Oct. 2009.

[18] A. Khaligh and M. D'Antonio, "Global trends in high-power on-board chargers for electric vehicles," *IEEE Trans. Veh. Technol.*, vol. 68, no. 4, pp. 3306–3324, Apr. 2019.

[19] S. Wang *et al.*, "Multifunction capability of SiC bidirectional portable chargers for electric vehicles," *IEEE J. Emerg. Sel. Topics Power Electron.*, vol. 9, no. 5, pp. 6184–6195, Oct. 2021, doi: 10.1109/JESTPE.2021.3052841.

[20] M. Kesler, M. C. Kisacikoglu, and L. M. Tolbert, "Vehicle-to-grid reactive power operation using plug-in electric vehicle bidirectional offboard charger," *IEEE Trans. Ind. Electron.*, vol. 61, no. 12, pp. 6778–6784, Dec. 2014.

[21] M. A. H. Rafi and J. Bauman, "A comprehensive review of dc fast-charging stations with energy storage: Architectures, power converters, and analysis," *IEEE Trans. Transport. Electrific.*, vol. 7, no. 2, pp. 345–368, Jun. 2021.

[22] C. Marxgut, J. Biela, and J. W. Kolar, "Interleaved triangular current mode (TCM) resonant transition, single phase PFC rectifier with high efficiency and high power density," in *Proc. Int. Power Electron. Conf. ECCE ASIA*, 2010, pp. 1725–1732.

[23] T. Soeiro, T. Friedli, and J. W. Kolar, "Three-phase high power factor mains interface concepts for electric vehicle battery charging systems," in *Proc. 27th Annu. IEEE Appl. Power Electron. Conf. Expo.*, 2012, pp. 2603–2610.

[24] C. Marxgut, F. Krismer, D. Bortis, and J. W. Kolar, "Ultraflat interleaved triangular current mode (TCM) single-phase PFC rectifier," *IEEE Trans. Power Electron.*, vol. 29, no. 2, pp. 873–882, Feb. 2014.

[25] A. M. Hava, R. J. Kerkman, and T. A. Lipo, "Simple analytical and graphical methods for carrier-based PWM-VSI drives," *IEEE Trans. Power Electron.*, vol. 14, no. 1, pp. 49–61, Jan. 1999.

[26] Dae-Woong Chung and Seung-Ki Sul, "Minimum-loss strategy for three-phase PWM rectifier," *IEEE Trans. Ind. Electron.*, vol. 46, no. 3, pp. 517–526, Jun. 1999.

[27] J. Xu, T. B. Soeiro, F. Gao, H. Tang, and P. Bauer, "Minimum switching losses discontinuous pwm strategy for bidirectional single-phase ac-dc converter with active power decoupling circuit," *IEEE Trans. Power Electron.*, vol. 36, no. 5, pp. 6118–6132, May 2021.

[28] T. D. Nguyen, J. Hobraiche, N. Patin, G. Friedrich, and J. P. Vilain, "A direct digital technique implementation of general discontinuous pulse width modulation strategy," *IEEE Trans. Ind. Electron.*, vol. 58, no. 9, pp. 4445–4454, Sep. 2011.

[29] J. Xu, J. Han, Y. Wang, M. Ali, and H. Tang, "High-frequency SiC three-phase VSIs with common-mode voltage reduction and improved performance using novel tri-state PWM method," *IEEE Trans. Power Electron.*, vol. 34, no. 2, pp. 1809–1822, Feb. 2019.

[30] J. Xu, J. Han, Y. Wang, S. Habib, and H. Tang, "A novel scalar PWM method to reduce leakage current in three-phase two-level transformerless grid-connected VSIs," *IEEE Trans. Ind. Electron.*, vol. 67, no. 5, pp. 3788–3797, May 2020.

[31] L. Schrittwieser, J. W. Kolar, and T. B. Soeiro, "99% efficient three-phase buck-type sic mosfet pfc rectifier minimizing life cycle cost in dc data centers," *CPSS Trans. Power Electron. Appl.*, vol. 2, no. 1, pp. 47–58, 2017.

[32] L. K. Ries, T. B. Soeiro, M. S. Ortmann, and M. L. Heldwein, "Analysis of carrier-based pwm patterns for a three-phase five-level bidirectional buck +boost-type rectifier," *IEEE Trans. Power Electron.*, vol. 32, no. 8, pp. 6005–6017, Aug. 2017.

[33] T. B. Soeiro, G. J. M. de Sousa, M. S. Ortmann, and M. L. Heldwein, "Three-phase unidirectional buck-type third harmonic injection rectifier concepts," in *Proc. IEEE Appl. Power Electron. Conf. Expo.*, 2014, pp. 928–934.

[34] Datasheet of C3M0120090J, *CREE Power Appl.*, Durham, NC, USA, Jan. 2018. [Online]. Available: https://www.wolfspeed.com/media/downloads/834/C3M0120090 J.pdf

[35] M. Haider *et al.*, "Novel zvs s-tcm modulation of three-phase ac/dc converters," *IEEE Open J. Power Electron.*, vol. 1, pp. 529–543, 2020, doi: 10.1109/OJPEL.2020.3040036.

[36] M. Antivachis, J. A. Anderson, D. Bortis, and J. W. Kolar, "Analysis of a synergetically controlled two-stage three-phase DC/AC buck-boost converter," *CPSS Trans. Power Electron. Appl.*, vol. 5, no. 1, pp. 34–53, Mar. 2020.

Junzhong Xu (Member, IEEE) was born in Ningbo, China, in 1994. He received the B.S. degree in electrical engineering from the Harbin Institute of Technology, Harbin, China, in 2016, and the Ph.D. degree in electrical engineering from Shanghai Jiao Tong University, Shanghai, China, in 2021.

From January 2020 to June 2021, he was a Visiting Scholar with the DC Systems, Energy Conversion and Storage Group, Delft University of Technology, Delft, the Netherlands. He is currently a Postdoctoral Research Fellow with the Department of Electrical Engineering, Shanghai Jiao Tong University. His research interests include advanced control and modulation for power converters.

Thiago Batista Soeiro (Senior Member, IEEE) received the B.S. (with Hons.) and M.S. degrees in electrical engineering from the Federal University of Santa Catarina, Florianopolis, Brazil, in 2004 and 2007, respectively, and the Ph.D. degree from the Swiss Federal Institute of Technology, Zurich, Switzerland, in 2012.

During the master's and Ph.D. studies, he was a Visiting Scholar with Power Electronics and Energy Research Group, Concordia University, Montreal, QC, Canada, and with the Center for Power Electronics Systems, Blacksburg, VA, USA, respectively. From 2012 to 2013, he was a Senior Engineer with the Power Electronics Institute, Federal University of Santa Catarina, Florianópolis, Brazil. From 2013 to 2018, he was a Senior Scientist with Corporate Research Center, ABB Switzerland Ltd., Switzerland. From 2018 to 2021, he was affiliated to the DC Systems, Energy Conversion and Storage Group, Delft University of Technology, Delft, The Netherlands, where he successfully acquired his Tenure Academic Position and was an Associate Professor of high power electronics. Since January 2022, he has been affiliated to the European Space Agency (ESA) with the European Space Research and Technology Centre (ESTEC), Noordwijk, the Netherlands, where he works on the R&D of power conditioning and distribution units for satellites.

Yong Wang (Member, IEEE) received the Ph.D. degree in power electronics from Zhejiang university, Hangzhou, China, in 2005.

From 2005 to 2008, he was a Senior Researcher with the Samsung Advanced Institute of Technology, Suwon, South Korea, working on the fuel cell grid tied inverter. From 2008 to 2010, he was with Danfoss Solar Inverters, Soenderborg, Denmark, as a Power Electronics Hardware Engineer. In the year 2010, he joined Shanghai Jiao Tong University, Shanghai, China, where he is currently a Full Professor with the Department of Electrical Engineering. His main research interests include grid-tied inverter technology, high frequency DC-DC converter based on wide bandgap devices applied in EV, and wireless power transfer.

Fei Gao (Member, IEEE) received the Ph.D. degree in electrical engineering from the Power Electronics Machines and Control (PEMC) Research Group, University of Nottingham, Nottingham, U.K., in 2016.

From March 2010 to September 2012, he was with Jiangsu Electric Power Research Institute, Nanjing, China, State Grid Corporation of China, Beijing, China. From 2016 to 2019, he was a Postdoctoral Researcher with the Department of Engineering Science, University of Oxford, Oxford, U.K. Since July 2019, he has been joined Shanghai Jiao Tong University, Shanghai, China, as an Associate Professor. His current research interests include modelling, control, power management and stability of microgrids, and more electric transportation systems.

Dr. Gao won the European Union Clean Sky Best Ph.D. Award in 2017 and IET Control and Automation Runner Up Ph.D. Award in 2018.

Houjun Tang received the Ph.D. degree in automation from Yamagata University, Yamagata, Japan, in 1997.

He is currently a Full Professor with the Department of Electrical Engineering, Shanghai Jiao Tong university, Shanghai, China. His research interests include wireless power transform, motor drive inverters, and power converters.

Pavol Bauer (Senior Member, IEEE) received the master's degree in electrical engineering from the Technical University of Kosice, Košice, Slovakia, in 1985, the Ph.D. degree from the Delft University of Technology, Delft, the Netherlands, in 1995, and title Prof. from the president of Czech Republic, Brno University of Technology, Brno, Czechia, in 2008, and Delft University of Technology, in 2016. He is currently a Full Professor with the Department of Electrical Sustainable Energy, Delft University of Technology and the Head of DC Systems, Energy Conversion and Storage Group. He has authored or coauthored more than 72 journal and about 300 conference papers in my field (with H factor Google scholar 43, Web of science 20), eight books, holds four international patents and organized several tutorials at the international conferences.

He has worked on many projects for industry concerning wind and wave energy, power electronic applications for power systems, such as Smarttrafo, HVDC systems, projects for smart cities, such as PV charging of electric vehicles, PV and storage integration, contactless charging, and he participated in several Leonardo da Vinci and H2020 EU Projects, as a Project Partner (ELINA, INETELE, E-Pragmatic) and Co-ordinator (PEMCWebLab.com-Edipe, SustEner, Eranet DCMICRO).